Available online at www.sciencedirect.com

jmr&t
Journal of Materials Research and Technology

journal homepage: www.elsevier.com/locate/jmrt

Original Article

Multi-scale structural and mechanical characterisation in bioinspired polyurethane-based pancreatic cancer model

Jingyi Mo [a,**], *Nathanael Leung* [a], *Priyanka Gupta* [b], *Bin Zhu* [a], *Hui Xing* [c], *Jiao Zhang* [c], *Eirini Velliou* [b,d], *Tan Sui* [a,*]

[a] *Bioinspired Materials Group, Department of Mechanical Engineering Sciences, University of Surrey, Guildford, Surrey, GU2 7XH, UK*

[b] *Bioprocess and Biochemical Engineering Group (BioProChem), Department of Chemical and Process Engineering, University of Surrey, Guildford, Surrey, GU2 7XH, UK*

[c] *School of Materials Science and Engineering, Shang Hai Jiao Tong University, Shang Hai, 200240, People's Republic of China*

[d] *Centre for 3D Models of Health and Disease, Division of Surgery and Interventional Science, University College London, London, W1W 7TY, UK*

ARTICLE INFO

Article history:
Received 5 May 2021
Accepted 9 September 2021
Available online 17 September 2021

Keywords:
Bioinspired polyurethane
Surface functionalisation
Synchrotron X-ray techniques
in situ mechanical testing

ABSTRACT

In this work, novel bioinspired polyurethane (PU) scaffolds were fabricated via freeze casting for PU-based Pancreatic Ductal Adenocarcinoma (PDAC) model. In order to reproduce the tumour micro-environment that facilitates cellular kinetics, the PU scaffolds were surface modified with extracellular matrix (ECM) proteins including collagen and fibronectin (Col and FN). Synchrotron-based small- and wide-angle X-ray scattering (SAXS/WAXS) techniques were applied to probe structural evolution during *in situ* mechanical testing. Strains at macroscopic, nano-, and lattice scales were obtained to investigate the effects of ECM proteins and pancreatic cell activities to PU scaffolds. Significant mechanical strengthening across length scales of PU scaffolds was observed in specimens surface modified by FN. A model of stiffness modulation via enhanced interlamellar recruitment is proposed to explain the multi-scale strengthening mechanisms. Understanding multi-scale deformation mechanisms of a series of PU scaffolds opens an opportunity in developing a novel pancreatic cancer model for studying cancer evolution and predicting outcomes of drug/treatments.

* Corresponding author.
** Corresponding author.
E-mail addresses: j.mo@surrey.ac.uk (J. Mo), t.sui@surrey.ac.uk (T. Sui).

https://doi.org/10.1016/j.jmrt.2021.09.041

1. Introduction

Pancreatic ductal adenocarcinoma (PDAC), the 14th frequent malignancy in the modern world, is an aggressive cancer with worldwide incidence of 460,000 cases in 2018 [1]. Despite a relatively low incident rate, in 2018 the PDAC-associated death toll is 430,000, making it the 7th leading cause of cancer-related death worldwide and 5th in the UK [2,3]. Once metastasised, its prognosis is extremely poor with a 5-year survival rate less than 8%, which has not experienced significant changes in the last few decades, even though intense research effort has been taken [4]. Such high disease mortality is mainly attributed to the lack of distinctive biomarkers for early stage diagnoses, as well as the complex extracellular matrix (ECM) of the tumour which facilitates the progression, treatment resistance and even recurrence [5,6].

Tissue engineering is a multidisciplinary subject involving biological materials (cells), polymers and engineering techniques with the aim of developing artificial models to mimic/replace biological tissues *in vitro*. This approach has also attracted cancer researchers' interests with a hope to develop *in vitro* tissue-engineered model for observing the physiological process of cancer evolution and predicting the clinical outcomes of drug screening. Two-dimensional (2D) *in vitro* system has been classically used for PDAC (re-)modelling [7–9], which however does not accurately simulate the three-dimensional (3D) *in vivo* characteristics of tumour micro-environments. Animal models are more accurate for PDAC research compared to 2D *in vitro* system and have been widely applied for chemoradiotherapy testing at selected disease's stage [7,10–12]. However, animal experiments are expensive, labour-intensive and time-consuming. Most importantly they are not always repeatable.

Criteria for 3D tissue-engineered scaffold for cancer research include biostability, interconnected porous structure facilitating the tumour micro-environment recapitulation [13–16] and appropriate surface properties enabling ECM mimicry for tumour development [16–18]. Additionally, the mechanical properties, e.g., tensile strength, are equally important as mechanical cues can trigger and modulate how the cell behaves [19,20]. Of the many different polymetric 3D systems that have been used in tissue engineering, polyurethane (PU) which provides easy control of internal structure (interconnectivity, size and shape of the pores) has emerged as one of the most promising candidates [13,14,21]. As an adjunct feature, surface properties of PU-based scaffolds can be custom-adjusted by surface modification using different ECM proteins, for instance collagen (Col) and fibronectin (FN), to reproduce the tumour micro-environment which favours cancer cell anchorage and treatment/drug responses [22,23]. However, in some cases PU may degrade under different device-specific conditions, such as cellular activities or loading conditions, and will impair mechanical stability and consequently lead to scaffold failure [24,25]. In order to optimise 3D PU-based scaffold design and avoid unexpected degradation and malfunction, so as to develop an appropriate *in vitro* tissue-engineered model to study the tumour-regulatory mechanisms and treatment/drug response, it is crucial to understand the relation between internal structure, mechanical properties, and their response to cellular activities.

The majority of research on PU-based scaffolds have been focusing on measuring and manipulating the bulk properties at the macroscopic level, the biomechanical and structural characteristics at different length scales have been neglected, which have been reported to be important in determining the efficiency of drug delivery into the tumour [13,21,23,26,27]. Moreover, measurement of mechanical properties both before and after the growth of cellular components is crucial to identify the biostability of the *in vitro* tissue-engineered model. Among the numerous experimental methods for studying the structural alteration of PU-based scaffolds, synchrotron X-ray techniques have been shown to be a very powerful tool for *in situ* multi-scale structural analysis for a series of polymeric materials, and allow probing of the intricate links between structural alteration and mechanical properties across the multiple length scales. Small-angle X-ray scattering (SAXS) is well-established for quantifying the structural evolution of both crystalline and amorphous phases of polymeric materials at the nanoscale whilst the wide-angle X-ray scattering (WAXS) has been widely applied in revealing the structural changes at the atomic level led by mechanical loading quantitatively [28–31].

In this work, both the mechanical properties in response to surface modification by ECM proteins (Col and FN) and pancreatic cell activities are investigated. In particular, the mechanical performance and the structural evolution of this bioinspired PU-based scaffold was explored at multiple length scales using *in situ* micromechanical testing with SAXS/WAXS. This provides an observational basis for improved insight into the structure–property relations for future design and development of the *in vitro* tissue-engineered model and its application in bioengineering and biomedical field such as therapeutic treatment.

2. Materials and Methods

2.1. Sample preparation

2.1.1. Polymer scaffold preparation and surface modification

Polymeric polyurethane (PU) scaffolds were produced using thermal induced phase separation (TIPS) method reported previously [21,23]. PU beads (EG-80A, molecular weight 148,474 g/mol, Noveon, Belgium) were dissolved in organic solvent dioxane (5% w/v) (99.8% anhydrous pure, Sigma–Aldrich, UK) then quenched at −80 °C for 3 h followed by solvent removal by freeze drying in a poly-ethylene glycol (PEG) bath at −15 °C. The chemical components of the hard segment (HS) and soft segment (SS) of the PU is shown in Fig. 1 (a). HS is comprised by a combination of hexamethylene diisocyanate (HMDI) and 1,4-butanediol (chain extender), and the SS is consisted of poly (tetrahydrofuran) (pTHF).

The scaffolds were then cut into 5 × 10 × 2.5 mm^3 cubes. They were then sterilized by dipping them in 70% ethanol (3 h) followed by UV ray exposure (1 h). As previously reported, the average pore size of the scaffolds was 100–150 μm and the porosity was 85–90% [16,32].

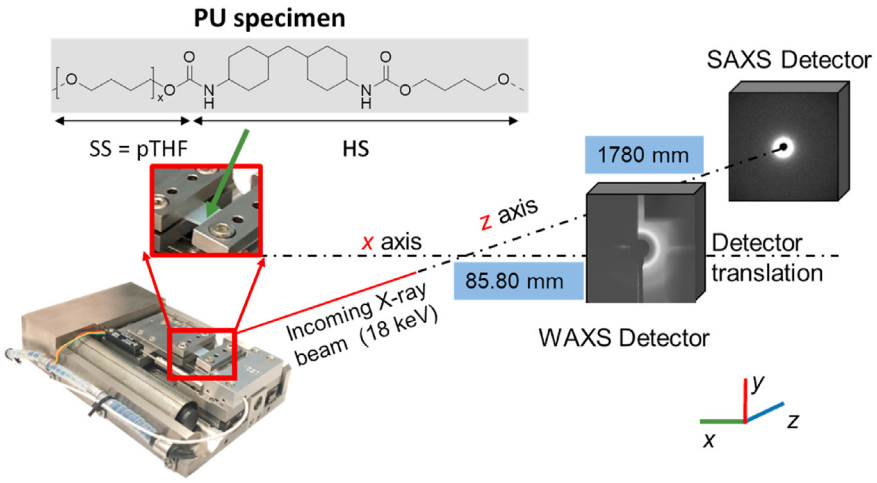

Fig. 1 – *In situ* experimental setup at beamline B16 Diamond Light Source incorporating a micromechanical rig, SAXS and WAXS detectors.

As previously described, the generated scaffolds were surface modified (adsorption) with fibronectin (Sigma–Aldrich, UK) and collagen I (Sigma–Aldrich, UK) for ECM mimicry. Briefly, the scaffolds were centrifuged in Phosphate Buffered Saline (PBS, Sigma–Aldrich, UK) for 10 min at 2500 rpm, followed by further centrifugation in fibronectin/collagen I solution (25 μg ml^{-1}) for 20 min at 2000 rpm. A final centrifugation in PBS for 10 min at 1500 rpm was carried out to unblock the scaffold pores.

2.1.2. *Cell culture on PU-based scaffolds*

The 3D cell culture was conducted as previously described [33]. The human pancreatic adenocarcinoma cell line PANC-1 (Sigma–Aldrich, UK) was expanded in Dulbecco's modified Eagle's medium (DMEM) with high glucose (Lonza, UK) supplemented with 10% fetal bovine serum (Fisher Scientific, UK), 1% penicillin/streptomycin (Fisher Scientific, UK) and 2 mM L-glutamine (Sigma–Aldrich, UK) in a humidified incubator at 37 °C with 5% CO_2. For all experimental conditions, 2×10^6 cells (re-suspended in 30 μl of cell culture media) were seeded in each scaffold. Immediately after seeding, the scaffolds were placed in the incubator for 1 h to promote cellular attachment within the scaffolds. Post 1 h incubation, 1.5 ml of cell culture media was added to each scaffold followed by incubation in a humidified incubator at 37 °C with 5% CO_2 for the entire duration of the experiment (2 weeks). The cell culture medium was changed every two days. At the end of the culture period, the scaffolds were fixed with 4% paraformaldehyde (SIGMA- Aldrich, Merck, UK), dried in a vacuum desiccator for further imaging and analysis. Uncoated PU scaffolds were used as control for all experiments.

2.1.3. *PU scaffolds for* in situ *micromechanical testing*

The sample selection consisted of three groups PU scaffolds: i) pure PU and PU seeded with cells (PU-Cell); ii) PU surface-modified with collagen (PU-Col) and PU surface-modified with collagen and seeded with cells (PU-Col-Cell); iii) PU surface-modified with fibronectin (PU-FN) and PU surface-modified with FN and seeded with cells (PU-FN-Cell). Specimens for *in situ* micromechanical testing combined with SAXS/WAXS were cut into rectangular shape, $10 \times 2.5 \times 5$ mm^3 in dimension (Table 1).

2.2. In situ *micromechanical with SAXS/WAXS*

The combined *in situ* micro-tensile mechanical testing with SAXS/WAXS experiment was performed on the B16 beamline at Diamond Light Source (DLS, UK). PU specimens mounted on the portable mechanical rig (Microtest, Deben Ltd., Suffolk, UK) were stretched at a constant displacement rate of 0.2 mm/min with a 200 N load cell. The schematic representation of the experimental setup is illustrated in Fig. 1. The Microtest tensile testing software was used to control and record the applied load and displacement. The slit-collimated monochromatic synchrotron X-ray beam (spot size 180×180 μm^2) with a wavelength of 0.6890 Å (X-ray beam energy 18.0 keV) was used to measure the scattering patterns. The SAXS and WAXS patterns were acquired continuously during the uniaxial deformation with an acquisition interval of 0.2 N. Each SAXS and WAXS pattern was collected in the plane perpendicular to the incident X-ray beam and parallel to the uniaxial loading direction. WAXS patterns were acquired with a Imagine Star 9000 detector (Photonic Science Ltd., UK) with a 500 ms exposure time at sample-detector-distance of 85.8 mm, as calibrated by a silicon standard. SAXS detector (Pilatus 300k, Dectris, Baden, Switzerland) was translated into the incident X-ray beam right after the WAXS measurement and the patterns were collected at sample-detector-distance of 1780 mm with an exposure time of 200 ms, as calibrated by a silver behenate (AgBh) standard.

Table 1 – Sample list.

Group No.	Description	
Group #1 Non-modified	Pure PU	PU-Cell
Group #2 Col-modified	PU-Col	PU-Col-Cell
Group #3 FN-modified	PU-FN	PU-FN-Cell

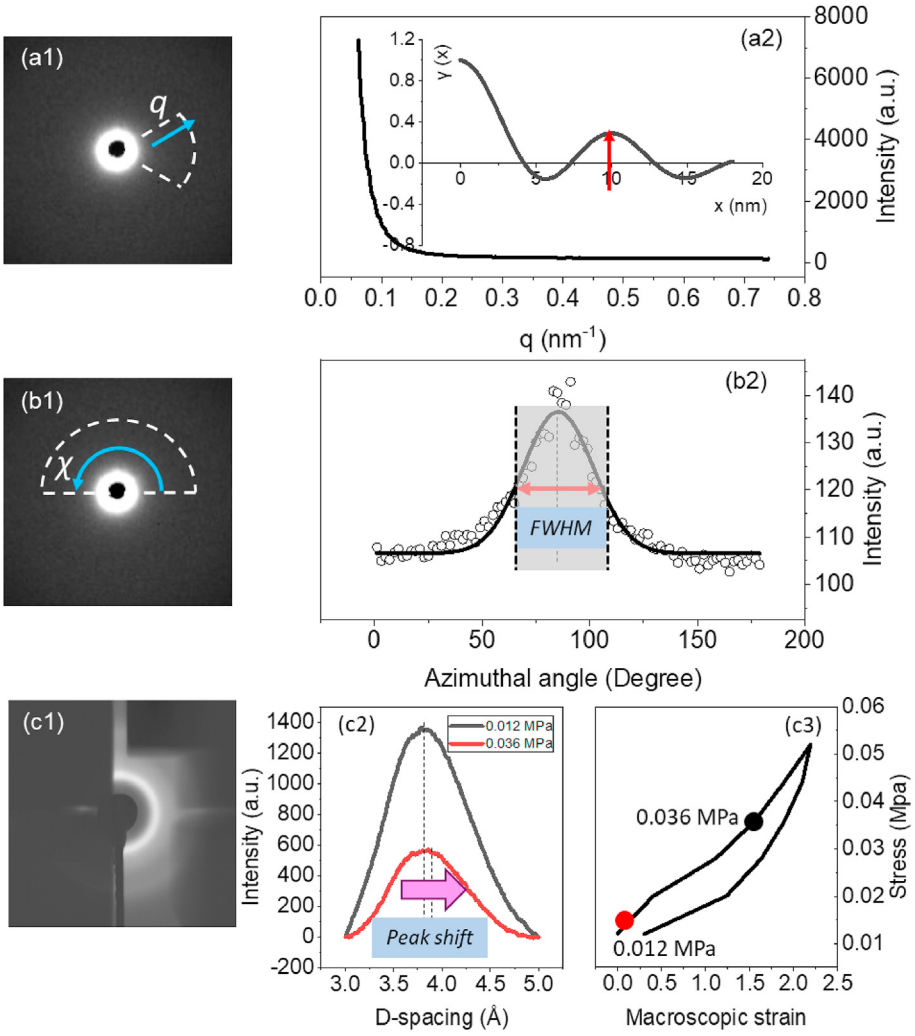

Fig. 2 – X-ray data reduction pipeline: (a1) A 2D SAXS pattern at 0 strain, dash lines denote the area where the azimuthal integration is performed. (a2) The 1D SAXS intensity profile (I(q)), inset shows corresponding 1D SAXS electron density correlation function for analysing nanostructural lamellae. (b1) The same 2D SAXS pattern as b1, radial integration is performed over the region denoted within the dash lines. (b2) The 1D SAXS intensity profile (I(χ)), experimental data (open circle) is fitted with Gaussian function as the guideline to eye, the FWHM marked by double-headed arrow. (c1) 2D WAXS pattern at the same strain level as in b1. (c2) The 1D integrated WAXS intensity profile (I(D)) after linear background subtraction for two levels of applied macroscopic strain at 0% (pink line), 1.7% (dark red line), showing the peak shift to the right as applied load increases. (c3) Macroscopic loading and unloading stress–strain plot for a pure PU specimen, with red and black dots indicating the position where the 1D WAXS profiles in (c2) are shown.

2.3. *Data processing and analysis*

2.3.1. *SAXS lamellae long period*

In SAXS, the scattering pattern results from the frequently occurring spacing of semi-crystal and amorphous lamellar stacks inside polymer. 2D SAXS patterns $I(q,\chi)$ (Fig. 2 (a1)) from Group #1 pure PU were processed by azimuthally integrating over angular range (χ) of ±20° using data analysis software package Fit2D [28,34]. Only the deformation of the lamellar stacks strained along the loading direction is being considered in the present study. The resultant 1D radial intensity profile $I(q)$ opens the door for solving the structural dimension so-called long period of the lamellae (Fig. 2 (a2)), where q is the length of the scattering vector $\underset{q}{\rightarrow}$. The peak representing the periodic stacking of lamellae is identified by converting the 1D radial intensity profile from reciprocal space to real space dimension through the following electron density function ($\gamma(x)$):

$$\gamma(x) = \int_0^\infty I(q)q^2 \cos qx \Big/ \int_0^\infty I(q)q^2 dq \qquad (1)$$

The apex corresponding to the average value of lamellae long period (L_P) is denoted by the red arrow in the inset graph of Fig. 2 (a2) and the position of this correlation peak ~10 nm is determined via Gaussian function fitting. The changes of L_P with respect to its strain-free state can be considered to be a strain measurement at the lamellar scale. The lamellae

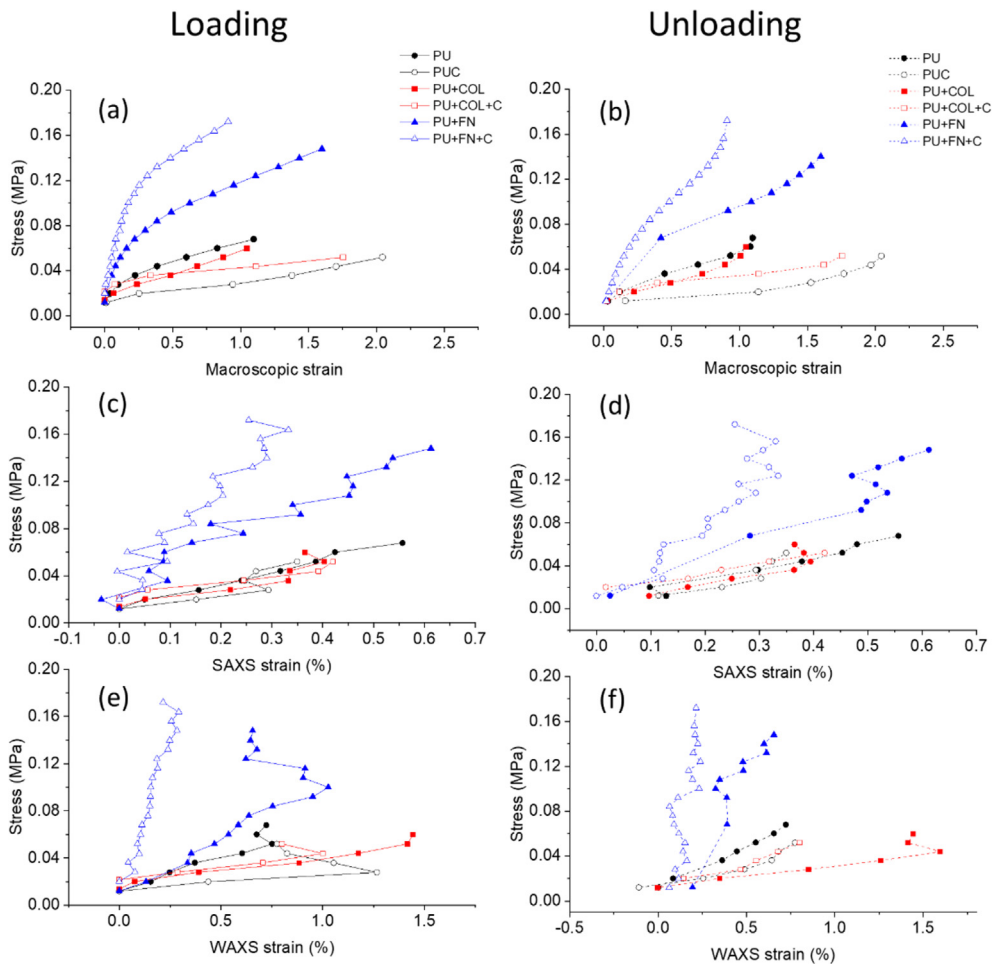

Fig. 3 – Altered multi-scale stress take-up in control, protein and cell treated PU specimens during loading and unloading cycle. (a,b) macroscopic stress-strain plots for Group #1 (pure PU, PU-Cell), Group #2 (PU-Col, PU-Col-Cell) and Group #3 (PU-FN, PU-FN-Cell) PU specimens during loading and unloading cycle. (c,d) Corresponding macroscopic tensile stress vs. SAXS strain curves and (e,f) corresponding macroscopic tensile stress vs. WAXS strain curves from PU with different treatments.

apparent moduli $\left(E_{Lp} = \frac{d\sigma_M}{d\varepsilon_{SAXS}}\right)$ calculated from the linear model fit of the macroscopic stress (σ_M) vs. lamellar strain (SAXS strain, ε_{SAXS}) curve are derived for quantifying the variations of nanomechanical parameter induced by surface modification and cell culture.

2.3.2. *SAXS domain orientation*

The predominant orientation of the lamella can also be extracted from the SAXS pattern. The angular distribution, which gives access to the orientational information of the rubbery lamellae, is calculated by integrating the same 2D SAXS pattern over the q range of 0.058 nm^{-1} to 0.074 nm^{-1}. Azimuthal angle (χ) is denoted with a dashed line from 0 to 180°, as shown in Fig. 2 (b2). The 1D SAXS azimuthal intensity profile I(χ) (solid circles) was fitted with a Gaussian function to determine the peak centre position χ_0 which defines the predominant orientation of the lamellae. The direction of lamellae ϕ in real space given by $\phi = \chi_0 \pm 90°$. The full width at half maximum (*FWHM*) signifies whether the angular distribution I(χ) is narrow or broad which reflects the degree of lamellar alignment: large *FWHM* indicates lower degree of alignment whilst *FWHM* will decrease as lamellar alignment increases.

2.3.3. *WAXS lattice strain*

An example 2D WAXS pattern from Group #1 pure PU is shown in Fig. 2 (c1). This 2D pattern (I(D, χ)) is azimuthally integrated across an angular sector of ±20° straddling the loading direction, resulting in a 1D WAXS intensity profile as a function of lattice *d*-spacing I(D). The WAXS intensity profile (after linear background subtraction) presented in Fig. 2 (c2) exhibits a lattice spacing of ~ 4 Å at the peak centre position. This observed amorphous halo corresponds to the overlying reflection of the urea moieties [35]. The WAXS intensity profile I(D) collected at the equivalent stress level of 0.012 MPa and 0.036 MPa (Fig. 2 (c3)) shows the peakcentre position shifts towards larger value of d-spacing under loading. In parallel to the increased d-spacing, the intensity of the scattering peak decreases which is partly due to the thinning down of the scattering volume with the application of loads. The lattice strain (WAXS strain, ε_{WAXS}), indicating the structural evolution at the atomic scale, could be derived from the percentage changes of peakcentre position with respect to the unstrained

state as reference. The lattice apparent moduli $\left(E_{LT} = \frac{d\sigma_M}{d\varepsilon_{WAXS}}\right)$ is defined as the slope obtained from the linear regression (σ_M) vs. WAXS strain (ε_{WAXS}) curve.

3. Results

Fig. 2 shows the 1D SAXS/WAXS (a2, b2 and c2) profiles for the control pure PU specimens at strain-free state. In the SAXS electron correlation function profile, a peak of ~10 nm is observed, indicating the thickness of the semi-crystalline and amorphous lamellae phase inside polymer. The correlation peak of 1D WAXS profile arises from periodic arrangement inside semi-crystalline phase is identified to be ~4 Å. As a result, it is conceivable that this type of PU is comprised of two distinct regions: a semi-crystalline domain with a characteristic period of ~4 Å, and rubbery amorphous lamellae. The overall length of these two regions, so called lamellae long period, is determined to be 10 nm by SAXS. At the nano- and atomic scale for SAXS and WAXS respectively, special attention is focused on the changes in lamellae long period and crystal lattice spacing during mechanical loading in order to probe the effects of surface modification on the mechanical behaviour of entangled lamellar network and the semi-crystalline phase, in the following sections.

The tensile mechanical testing was carried out to investigate the effects of Col and FN on the mechanical properties of the PU scaffold. The macroscopic stress (σ_M) vs. strain (ε_M) curves of PU scaffolds with different treatments, including pure PU (solid black), PU-Cell (open black), PU-Col (solid red), PU-Col-Cell (open red), PU-FN (solid blue) and PU-FN-Cell (open blue), were plotted in Fig. 3 (a,b), showing a classic non-linear mechanical behaviour of polymer macroscopically. From Fig. 3 (c–f), it is clear that FN has a stiffening effect on PU as Group #3 (FN-modified) shows steeper slope in the macroscopic stress σ_M vs. strain ε_M curve compared to the non-modified groups. Comparing Group #1 (pure PU) and #2 (PU-Col), it appears that the cell culture leads to an increase in ductility. Overall, the PU-FN specimens are proved to be the stiffest whilst the PU-Cell specimens are the most ductile.

To demonstrate stress-induced multi-scale structural changes, the parameters i) lamellar strain (SAXS strain) (ii) lattice strain (WAXS strain) and iii) lamellar alignment as described previously in Materials and Methods are considered. For i) and ii), in Fig. 3 (c–f) it is shown that the structural units of PU at the lamellar and lattice scale with different treatments—non-modified, FN-modified and Col-modified—exhibit a different level straining at the same level of macroscopic stress σ_M. In Fig. 3 (c,d), the intrinsic mechanical behaviour of the amorphous lamellae during the loading and unloading cycle is presented. At a given stress of 0.05 MPa, we can observe that SAXS strain in PU-Cell (~0.3%) is quite close to PU-Col-Cell (~0.4%), whilst the strain in PU-FN-Cell is much lower (~0.09%). This reduction in strains developed at the lamellar level is likely due to the alteration in entangled lamellar networks mediated by FN (Fig. 3 (c)). The variations of WAXS strain in relation to surface modification is plotted in Fig. 3 (e,f). Consistent with what has been identified at the macroscopic and lamellar level, the WAXS strain exhibits a surprising upswing in the PU-FN-Cell group. This stiffening effect of FN is observed at multiple scales, as judged by the steeper inclination of the stress vs. strain plot of Group #3 (FN-modified, blue curves) shown in Fig. 3. Another observation to note is that the fairly linear increase of WAXS strain with macroscopic stress can only be observed in the case of PU-FN-Cell. For non-modified and Col-modified group it appears the WAXS strain starts to decrease beyond certain level of stress, which indicates that there is some form of atomic debonding occurring. Surprisingly, the precise form of this debonding appears to be such that the drops in macroscopic and SAXS strain do not yet occur, suggesting that the reduced stress carrying ability is initialising at the lattice scale.

In order to quantitatively interpret the mechanical parameter in a multi-scale manner, we consider the Young's moduli for macroscopic stress vs. macroscopic strain and 'apparent moduli' that corresponds to the slope of each macroscopic stress vs. SAXS/WAXS strain curve. Progressing from the observational trends in the representative specimen from each group as illustrated in Fig. 3, the alterations of the Young's moduli and the lamellae and lattice apparent moduli pooled across specimens with different treatments are demonstrated and the evolution of strain at multiple length scales over the loading cycle is compared in Fig. 4. Macroscopically, the qualitative impression of higher slopes in FN-modified group is confirmed by the linear model fits of the stress vs strain plots. PU-Col-Cell (n = 3; 0.016 ± 0.001 MPa) has roughly a 50% smaller Young's moduli compared to PU-Cell (n = 3; 0.03 ± 0.002 MPa), whilst PU-FN-Cell (n = 3; 0.107 ± 0.063 MPa) is over three times larger (Fig. 4 (a)). At the nano-scale, comparing with lamellar apparent moduli in PU-FN-Cell (n = 2; 41.6 ± 1.4 MPa), the PU-Cell (n = 2;

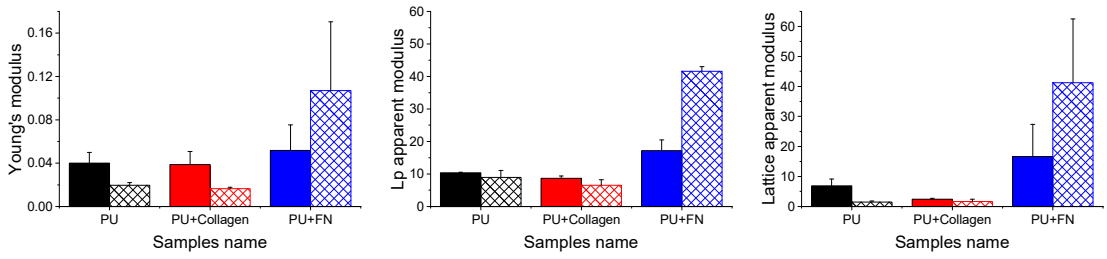

Fig. 4 – Quantified multi-scale mechanics of PU. (a) Averaged Young's moduli (b) lamellae apparent moduli calculated from macroscopic stress vs. SAXS strain (c) and the lattice apparent moduli calculated from macroscopic stress vs. WAXS strain curves for Group #1 (PU, PUC), Group #2 (PU-Col, PU-Col-Cell) and Group #3 (PU-FN, PU-FN-C).

8.9 ± 2.2 MPa) and PU-Col-Cell (n = 2; 6.5 ± 1.7 MPa) are ~79% and 84% less respectively (Fig. 4 (b)). Consistent with the results in the cell-seeded group, a notable stiffening phenomenon by FN can also be observed in the cell-free group. For example, PU-FN (n = 2; 17.2 ± 3.3 MPa) shows a ~70% increase of lamellar apparent moduli when compared to the control group (pure PU; n = 3; 10.4 ± 0.2 MPa). In terms of strain at lattice scale, it is found in Fig. 4 (c) that the PU-FN-Cell (n = 2; 41.2 ± 21.2 MPa) has the highest lattice apparent moduli, whilst PU-Col-Cell (n = 2; 1.6 ± 0.8 MPa) is slightly larger (~10%) relative to the PU-Cell (n = 2; 1.5 ± 0.4 MPa). A similar increase of lattice apparent moduli induced by FN can also be identified in the cell-free group at the lattice scale. The addition of cell to FN-modified PU leads to the significant increases in the Young's moduli and the lamellar and lattice apparent moduli, suggesting that FN-induced stiffening of PU is highly cell-dependent.

To understand how the stress and strain are transmitted through the semi-crystalline phase and amorphous lamellae and their relation to surface modification, we quantified the strain magnitude depending on the length scale as summarised in Table 2. In the cell-populated group, the proportionality factor between the SAXS and the macro strains ($\varepsilon_{SAXS}/\varepsilon_M$) in PU-FN-Cell (0.0041 ± 0.0012) is greater than PU-Col-Cell (0.0025 ± 0.0012), whilst PU-Cell (0.0027 ± 0.0024) is in between of these two. Concurrently in Group #3 (FN-modified), whilst the value of $\varepsilon_{WAXS}/\varepsilon_M$ in PU-FN is ~0.0085, after cell culture the value increases to ~0.0222, marking an overall increase of ~160%. Similar changes of increased strain ratio can be found at the lamellar level ($\varepsilon_{SAXS}/\varepsilon_M$) which dictates that this effect of cell can be observed throughout multiple length scales in FN-modified group. Such increased SAXS strain take-up in PU-FN-Cell demonstrates that the increased loads are being transferred in adjacent lamellae and lattice throughout the mechanical loading compared with PU-FN, which could be explained by the increased interlamellar cohesion. Conversely, in Group #2 (Col-modified), an opposite effect of cell is observed: reduced values of $\varepsilon_{SAXS}/\varepsilon_M$ and $\varepsilon_{WAXS}/\varepsilon_M$ in PU-Col-Cell are found, indicating that the addition of cell lowers the efficiency of load transfer from lamellar down to lattice level. In Group#1, it is noting that the proportionality factor of $\varepsilon_{SAXS}/\varepsilon_M$ in PU-Cell (0.0027 ± 0.0024) is lower than $_{p}$ure PU (0.0038 ± 0.0009) whilst proportionality factor of $\varepsilon_{WAXS}/\varepsilon_M$ changes in the opposite direction after the cell culture. However, given the existing large dispersion from the mean of $\varepsilon_{SAXS}/\varepsilon_M$ in PU-Cell, it cannot be concluded whether the cell culture had an effect on lowering the efficiency of load transferring at the lamellar scale.

Being concomitant with the elongation and extension of lamellae long period and lattice d-spacing, there are also marked alterations in *FWHM* (indicating the lamellar alignment) of SAXS I(χ) throughout the mechanical testing. The overall trend lamellar alignment is similar in both loading and unloading cycle, nevertheless, clear differences appear between different surface modifications, as shown in Fig. 5. The monotonic decrease of *FWHM* with increasing stress is observed both in Group #1 (non-modified) and #2 (Col-modified). This reduced *FWHM* indicates of a large distribution of randomly ordered lamellae stacks quickly aligned as stress increases. In contrast, for lamellae stacks in FN-modified Group #3, the *FWHM* increases with stress up to the transitional point of ~0.12 MPa, indicating an increased structural randomness, followed by the *FWHM* decrease to a minimum to ~60 (Fig. 5 (a)).

The cartoon schematics reflecting the orientational changes with the applied loads are proposed in Fig. 6 to compare the changes of *FWHM* between the control group (pure PU) and stiffened (FN-modified) cases. Fig. 6 (a) shows a representative *FWHM* at a strain-free state which exhibits a relatively small value ~60 (obtained from peak II) and then an increase to a maximum of 75 at 0.8 strain. The distribution is relatively broad with two peaks centering roughly at 90° and 130° (corresponds to lamellar direction of ~0° and 50° along the loading direction) in the unstrained state, then the two peaks merge together under loads, followed by a broader distribution with single peak centering roughly at 90°. For macroscopic strain greater than 0.8, the *FWHM* decreases monotonically—without discontinuous transition—as the strain increases. The increase of *FWHM* from 0 to 0.8 strain implies an increase of orientational randomness, as illustrated in the schematic representation shown in upper Fig. 6 (a–c), and may be due to the two lamellae orientations moving into a single broad orientation along the loading direction. The angular distributions and the schematic representations from the control group (pure PU) at two strain levels is similar to the FN-modified group, yet clear difference is proposed in the unstrained case. The pure PU exhibits single angular distribution at strain-free state (Fig. 6d). The elimination of the two peaks distribution is likely due to the initial load applied prior to the loading up. Note, the transitional position of the increase and the subsequent reduction of *FWHM* can only be found in FN-modified group, suggesting that the ability of reorientation (from the initial distribution with two main directions to a random and then highly oriented distribution) is lower for the stiffened PU.

Table 2 – Multi-scale strain ratio.

Group No.	Description	$\varepsilon_{SAXS}/\varepsilon_M$	$\varepsilon_{WAXS}/\varepsilon_M$
Group #1	PU	0.0038 ± 0.0009	0.0077 ± 0.0049
	PU-Cell	0.0027 ± 0.0024	0.0147 ± 0.0021
Group #2	PU-Col	0.0037 ± 0.0013	0.0153 ± 0.0033
	PU-Col-Cell	0.0025 ± 0.0012	0.0103 ± 0.0034
Group #3	PU-FN	0.0030 ± 0.0008	0.0085 ± 0.0087
	PU-FN-Cell	0.0041 ± 0.0012	0.0222 ± 0.0270

4. Discussions

In this work, we present an *in situ* multiple-length-scale deformation analysis using synchrotron-based SAXS/WAXS for a series of bioinspired PU-based pancreatic cancer models. Prior to the characterisation of mechanical and morphological properties, PU was coated with two different ECM proteins: Col and FN, which has been proved to be capable of enhancing the cell attachment to the polymer substrates [36–40]. This PU is a soft material with excellent ductility as measured by a stress of ~0.04 MPa at ~210% strain in PU-Cell group. FN-modification contributes a higher mechanical resistance to deformation in PU, as shown by the increase in maximum

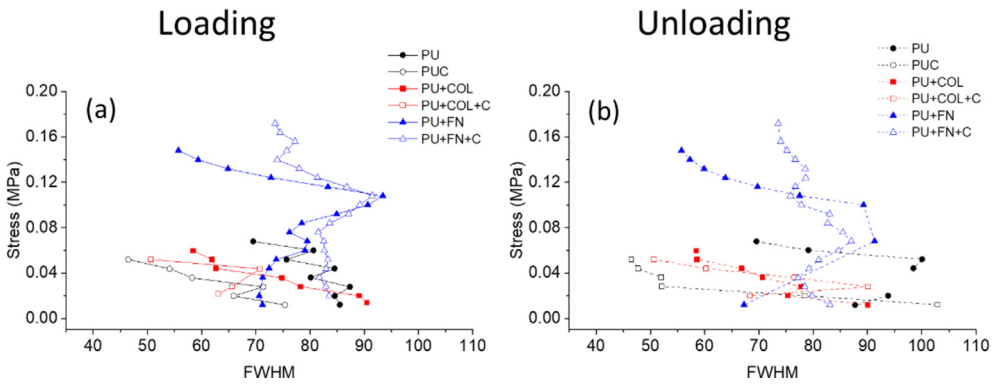

Fig. 5 – Altered lamellar alignment in Group #1 (PU, PU-Cell), Group #2 (PU-Col, PU-Col-Cell) and Group #3 (PU-FN, PU-FN-Cell) PU specimens during loading (a) and unloading cycle (b).

stress and the reduction in macroscopic strain during tensile deformation, both with and without the presence of cell. The increased tensile strength is likely due to the formation of an entangled network of FN fibrils on the scaffold surface, which can effectively mediate the mechanical properties macroscopically [36]. Such stiffening effect is manifested across length scales, as evidenced by the striking increase of apparent lamellar and lattice moduli induced by FN in Fig. 4. In Group #3 (FN-modified), the cell-seeded scaffold exhibits a higher-level of moduli at multiple length scales compared to the cell-free counterpart, possibly due to increased interlamellar cohesion led by enhanced cell adhesion [23,39]. Such alteration of interfacial properties would lead to an increased load-bearing capacity as observed in FN-modified specimens. In Group #2 (Col-modified), we also noted that cell culture lowers the tensile mechanical properties of PU scaffold throughout length scales. It is conjured that in this scenario, excessive matrix metallopeptidases (MMPs) were secreted from cells, followed by a degradation of structural proteins (e.g. collagen) [41], which in return lowers the interlamellar cohesion. It is known that cell-associated MMPs can mediate the cellular microenvironment remodelling [42,43]. However, the precise dynamic interplay between the ECM degradation, surface modification and ECM protein secretion are still poorly understood. For instance, the quantitative investigation about appropriate surface absorption time of collagen before the ECM microenvironment or metalloprotease level could significantly change the moduli of PU scaffold to date is still lacking. Further studies are required to assess and understand the cell-mediated ECM degradation and protein absorption on PU scaffold so that the appropriate surface functionalisation protocol can be established.

In support to these claims, it is worth looking into the strain ratio at multiple length scales during the tensile mechanical testing. The deformation along the loading direction where the semi-crystalline and lamellar phase are straining fairly in the same magnitude suggests that their arrangements obey a paralleled coupling, as illustrated in the schematic representation in Fig. 6 (d). A more efficient shear force transferring in the amorphous chain leads to a greater SAXS and WAXS strain take-up in Group #3 ($\varepsilon_{SAXS}/\varepsilon_M = 0.0041 \pm 0.0012$ and $\varepsilon_{WAXS}/\varepsilon_M = 0.0222 \pm 0.0270$) as shown in Fig. 6. It is possible that the increased interlamellar entanglements and cohesion led by FN fibrils and cellular activity are acting like a 'load-transmitter', transferring the applied loads between lamellae effectively. In contrast, in Group #2 (Col-modified) a significant decrease in both $\varepsilon_{SAXS}/\varepsilon_M$ and $\varepsilon_{WAXS}/\varepsilon_M$ is identified after cell culture. Such reduction in strain ratio complements the decreased load-bearing capacity after cell culture observed in Fig. 4 (Group #2) and taking together means a reduction in interfacial cohesion. This is another indirect evidence showing that the interconnections between adjacent lamellae build-up by collagen fibrils may be degraded by the cell-secreted MMPs. For electron spun bio-inspired PU film, the ratio between SAXS strain and macroscopic strain has been estimated to be ~0.3 [29,30], which is ~70 folds larger than the value reported here. Such differences may be resulted from the distinct nanostructure formed during different fabrication methods: freeze casting or electron spun. Instead, the ratio of WAXS strain and macroscopic strain of electron spun PU (~0.1) [29,30] is comparable with the value (0.022 ± 0.027) identified in the current study.

These experimental results from SAXS and WAXS allow to explain the structural changes induced by surface modification, in which interesting deformation mechanism was captured both before and after the growth of cellular components. On the basis of these experimental observations, a simple schematic model that sheds light on the key biophysical mechanisms enabling mechanically-tuneable PU is proposed in Fig. 6, which helps to complement data pertaining to the structural evolution and deformation at multiple length scales when PU was surface-modified differently. At the ultrastructural level, the lamellar stack in parallel with semi-crystalline of unmodified and FN-modified PU is illustrated as shown in Fig. 6 (f). Structurally, we considered that the anisotropic lamellae are embedded in the entangled interlamellar networks. Under mechanical loading, the mismatch in mechanical strength between the lamellae and the interlamellar networks will result in an inhomogeneous stress distribution, which will finally lead to the occurrence of a strong shear field in the interface. The FN-modification onto PU interlamellar networks is shown in Fig. 6 (f, upper), and can be considered as the representation of an increased entanglement as mentioned previously. In this manner, the alteration in interlamellar interface combined with the efficient shear load transmission enables the stiffening of PU scaffolds,

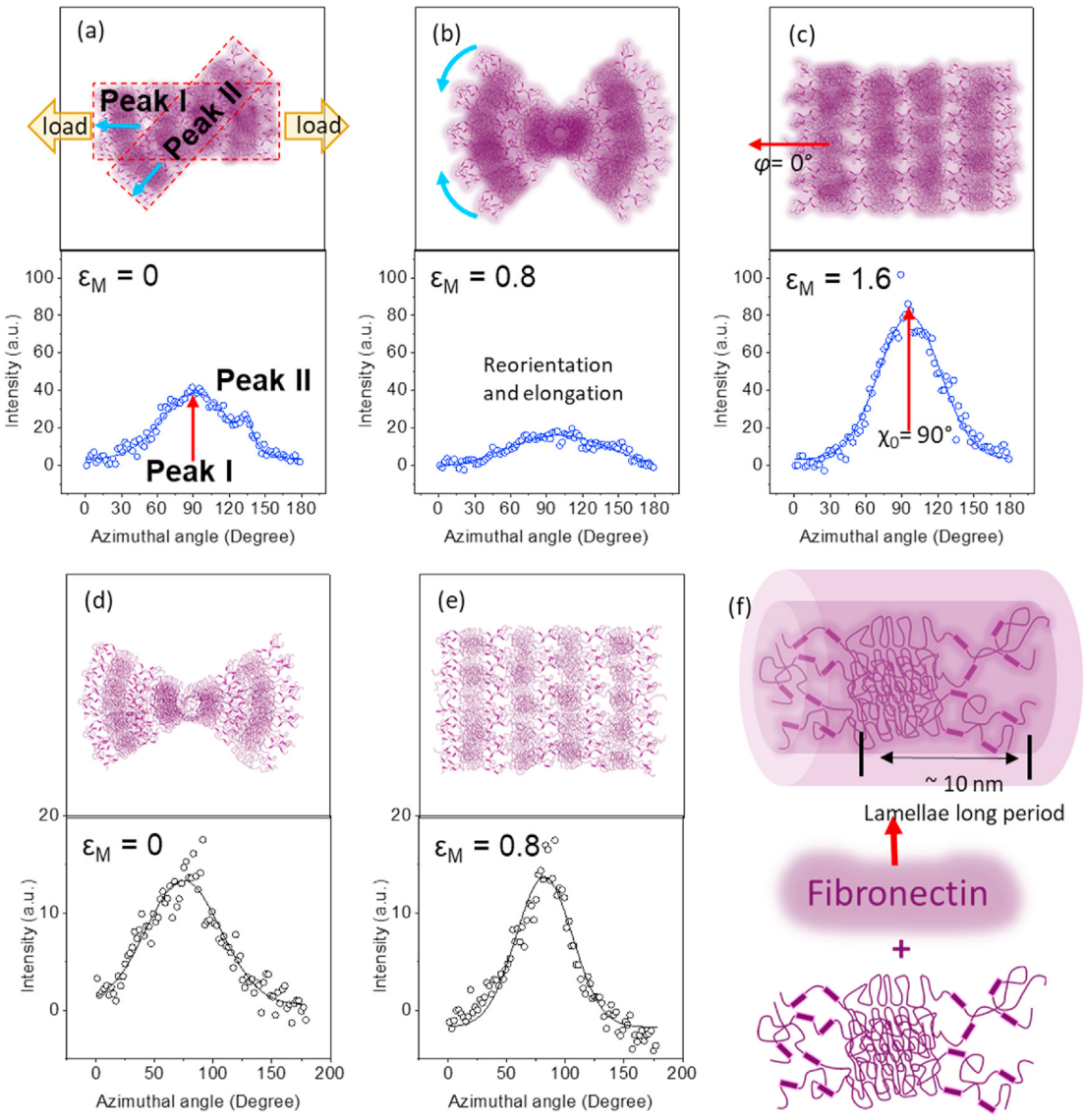

Fig. 6 – The reorientation and straining of lamellae in control and stiffened state: (a-c, upper) schematic representations demonstrate the lamellae from PU-FN reorienting and straining. The horizontal arrow in (a, upper) denotes the loading direction. (a-c, bottom) corresponding I(χ) profiles at three different strain levels. (a) At $\varepsilon_M = 0$, the I(χ) profile displays a bimodal distribution (peak I and II) arising from two groups of lamellae with two different orientation. (b) At $\varepsilon_M = 0.8$, a broader distribution of I(χ) due to lamellae progressively reorienting towards the loading direction (small *FWHM*) and (c) At $\varepsilon_M = 1.6$, a narrower distribution of I(χ) shows highly aligned lamellae (larger *FWHM*). (d and e, upper) schematic representations illustrate the lamellar structural evolution from pure PU. In (d and e, bottom), the I(χ) profile starts from single gaussian distribution from $\varepsilon_M = 0$ (d, bottom) with relatively wider I(χ) distribution and progressively reorienting to a highly aligned lamellar along the loading direction (larger *FWHM*) as shown in (e, bottom). (f) Schematic illustration of FN-induced strengthening via enhancing interlamellar cohesion.

as elucidated in Fig. 4. Along the loading direction, slight alteration in the interlamellar networks at the lamellar and lattice scale will amplify to massive changes in macroscopic stress, as a result of which the stress is much more efficiently conferred between adjacent lamellae. Reorientation of lamellar stacks towards the loading direction occurs simultaneously with the lamellar elongation and extension. However, in the lateral direction which is perpendicular to the tensile direction, the FN-modified specimens exhibits lower rate of lamellae recruitment to bear load, as shown by the transitional point of an increase of *FWHM* up to ~0.12 MPa and a subsequent decrease afterwards in Fig. 5, which would be attributed to the repulsion of the FN layer that detains the reorientation of lamellae.

5. Conclusions

In summary, in this first direct measurement of multi-scale deformation mechanisms of bioinspired PU scaffolds of

pancreatic cancer model using *in situ* combined micro-mechanical testing and SAXS/WAXS, we have shown the mechanical properties at the micro-, nano- and lattice scale for a series of PU specimens, including pure PU, PU-Cell, PU-Col, PU-Col-Cell, PU-FN and PU-FN-Cell. A greater lamellar recruitment, modulated by the entangled lamellar networks, results in a 4.5 folds increase of macroscopic stiffness. FN was found to be the optimal protein increasing in both the cell attachment and mechanical properties. Col is also found to be able to promote cellular activity but lower the mechanical properties of PU scaffold in comparison to FN possibly due to the excessive secretion of MMP in the tumour micro-environment. The use of *in situ* micromechanical testing combined with synchrotron X-ray techniques has allowed us to quantitatively measure both the deformation mechanics and the mechanical properties of constructive components at multiple length scales as PU undergoes different surface modifications. Understanding how these ECM proteins, FN and Col, interact with cells and the surface of polymer highlights the potential of tailoring the freeze-casted PU scaffold by combining both Col and FN to optimise biocompatibility and mechanical performance thereby develop a novel 3D tissue-engineered scaffold for PDAC research.

Declaration of Competing Interest

The authors declare that they have no known competing financial interests or personal relationships that could have appeared to influence the work reported in this paper.

Acknowledgements

We thank Dr Igor Dolbnya, from the B16 beamlines at Diamond Light Source (DLS), for his support and assistance with experimental setup and data acquisition. DLS is also acknowledged for providing access to the B16 beamline under the allocation MT20046. HX and JZ acknowledge support from the National Natural Science Foundation of China (No. 51627802 & No. 51871152). PG is supported by the Commonwealth Rutherford Post-Doctoral Fellowship as well as funding from the 3DbioNet. EV is grateful to the Royal Academy of Engineering for an Industrial Fellowship. TS and JM acknowledge support from Engineering and Physical Sciences Research Council (EP/S022813/1).

REFERENCES

[1] Bray F, Ferlay J, Soerjomataram I, Siegel RL, Torre LA, Jemal A. Global cancer statistics 2018: GLOBOCAN estimates of incidence and mortality worldwide for 36 cancers in 185 countries. CA Cancer J Clinic 2018;68(6):394–424.

[2] Smith RA, Andrews KS, Brooks D, Fedewa SA, Manassaram-Baptiste D, Saslow D, et al. Cancer screening in the United States, 2018: a review of current American Cancer Society guidelines and current issues in cancer screening. CA Cancer J Clin 2018;68(4):297–316.

[3] Torre LA, Trabert B, DeSantis CE, Miller KD, Samimi G, Runowicz CD, et al. Ovarian cancer statistics. CA Cancer J Clin 2018;68(4):284–96.

[4] Adamska A, Domenichini A, Falasca M. Pancreatic ductal adenocarcinoma: current and evolving therapies. Int J Mol Sci 2017;18(7):1338.

[5] Barker HE, Paget JT, Khan AA, Harrington KJ. The tumour microenvironment after radiotherapy: mechanisms of resistance and recurrence. Nat Rev Cancer 2015;15(7):409–25.

[6] Whatcott CJ, Posner RG, Von Hoff DD, Han H. Desmoplasia and chemoresistance in pancreatic cancer. In: Pancreatic cancer and tumor microenvironment. Transworld Research Network; 2012.

[7] Dovzhanskiy DI, Arnold SM, Hackert T, Oehme I, Witt O, Felix K, et al. Experimental in vivo and in vitro treatment with a new histone deacetylase inhibitor belinostat inhibits the growth of pancreatic cancer. BMC Cancer 2012;12(1):226.

[8] Harikumar KB, Kunnumakkara AB, Sethi G, Diagaradjane P, Anand P, Pandey MK, et al. Resveratrol, a multitargeted agent, can enhance antitumor activity of gemcitabine in vitro and in orthotopic mouse model of human pancreatic cancer. Int J Cancer Res 2010;127(2):257–68.

[9] Onishi H, Morifuji Y, Kai M, Suyama K, Iwasaki H, Katano M. Hedgehog inhibitor decreases chemosensitivity to 5-fluorouracil and gemcitabine under hypoxic conditions in pancreatic cancer. Cancer Sci 2012;103(7):1272–9.

[10] Awasthi N, Kronenberger D, Stefaniak A, Hassan MS, von Holzen U, Schwarz MA, et al. Dual inhibition of the PI3K and MAPK pathways enhances nab-paclitaxel/gemcitabine chemotherapy response in preclinical models of pancreatic cancer. Cancer Lett 2019;459:41–9.

[11] Courtin A, Richards FM, Bapiro TE, Bramhall JL, Neesse A, Cook N, et al. Anti-tumour efficacy of capecitabine in a genetically engineered mouse model of pancreatic cancer. PloS One 2013;8(6).

[12] Heinemann V, Haas M, Boeck S. Neoadjuvant treatment of borderline resectable and non-resectable pancreatic cancer. Ann Oncol 2013;24(10):2484–92.

[13] Totti S, Vernardis SI, Meira L, Pérez-Mancera PA, Costello E, Greenhalf W, et al. Designing a bio-inspired biomimetic in vitro system for the optimization of ex vivo studies of pancreatic cancer. Drug Discov Today 2017;22(4):690–701.

[14] O'brien FJ. Biomaterials & scaffolds for tissue engineering. Mater Today 2011;14(3):88–95.

[15] Ricci C, Mota C, Moscato S, D'Alessandro D, Ugel S, Sartoris S, et al. Interfacing polymeric scaffolds with primary pancreatic ductal adenocarcinoma cells to develop 3D cancer models. Biomatter 2014;4(1):e955386.

[16] Blanco TM, Mantalaris A, Bismarck A, Panoskaltsis N. The development of a three-dimensional scaffold for ex vivo biomimicry of human acute myeloid leukaemia. Biomaterials 2010;31(8):2243–51.

[17] Lu P, Weaver VM, Werb Z. The extracellular matrix: a dynamic niche in cancer progression. Int J Cell Biol 2012;196(4):395–406.

[18] Zeugolis DI, Paul GR, Attenburrow G. Cross-linking of extruded collagen fibers—a biomimetic three-dimensional scaffold for tissue engineering applications. J Biomed Mater Res A 2009;89(4):895–908.

[19] Lacroix D, Prendergast P. A mechano-regulation model for tissue differentiation during fracture healing: analysis of gap size and loading. J Biomech 2002;35(9):1163–71.

[20] Prendergast P, Huiskes R, Søballe K. Biophysical stimuli on cells during tissue differentiation at implant interfaces. J Biomech 1997;30(6):539–48.

[21] Gupta P, Totti S, Pérez-Mancera PA, Dyke E, Nisbet A, Schettino G, et al. Chemoradiotherapy screening in a novel

biomimetic polymer based pancreatic cancer model. RSC Adv 2019;9(71):41649–63.
[22] Velliou EG, Dos Santos SB, Papathanasiou MM, Fuentes-Gari M, Misener R, Panoskaltsis N, et al. Towards unravelling the kinetics of an acute myeloid leukaemia model system under oxidative and starvation stress: a comparison between two-and three-dimensional cultures. Bioproc Biosyst Eng 2015;38(8):1589–600.
[23] Totti S, Allenby MC, Dos Santos SB, Mantalaris A, Velliou EG. A 3D bioinspired highly porous polymeric scaffolding system for in vitro simulation of pancreatic ductal adenocarcinoma. RSC advances 2018;8(37):20928–40.
[24] Anderson JM, Hiltner A, Wiggins MJ, Schubert MA, Collier TO, Kao WJ, et al. Recent advances in biomedical polyurethane biostability and biodegradation. Polym Int 1998;46(3):163–71.
[25] Szycher M. Biostability of polyurethane elastomers: a critical review. J Biomater Appl 1988;3(2):297–402.
[26] Engler AJ, Sen S, Sweeney HL, Discher DE. Matrix elasticity directs stem cell lineage specification. Cell 2006;126(4):677–89.
[27] Ansari D, Friess H, Bauden M, Samnegård J, Andersson R. Pancreatic cancer: disease dynamics, tumor biology and the role of the microenvironment. Oncotarget 2018;9(5):6644.
[28] Sui T, Salvati E, Zhang H, Nyaza K, Senatov FS, Salimon AI, et al. Probing the complex thermo-mechanical properties of a 3D-printed polylactide-hydroxyapatite composite using in situ synchrotron X-ray scattering. J Adv Res 2019;16:113–22.
[29] Sui T, Salvati E, Ying S, Sun G, Dolbnya I, Dragnevski K, et al. Strain softening of nano-scale fuzzy interfaces causes Mullins effect in thermoplastic polyurethane. Sci Rep 2017;7(1):1–9.
[30] Sui T, Baimpas N, Dolbnya IP, Prisacariu C, Korsunsky AM. Multiple-length-scale deformation analysis in a thermoplastic polyurethane. Nat Commun 2015;6(1):1–9.
[31] Zhou C, Li H, Zhang W, Li J, Huang S, Meng Y, et al. Direct investigations on strain-induced cold crystallization behaviour and structure evolutions in amorphous poly (lactic acid) with SAXS and WAXS measurements. Polymer 2016;90:111–21.
[32] Safinia L, Mantalaris A, Bismarck A. Nondestructive technique for the characterization of the pore size distribution of soft porous constructs for tissue engineering. Langmuir 2006;22(7):3235–42.
[33] Gupta P, Pérez-Mancera PA, Kocher H, Nisbet A, Schettino G, Velliou EG. A novel scaffold-based hybrid multicellular model for pancreatic ductal adenocarcinoma—toward a better mimicry of the in vivo tumor microenvironment. Front Bioeng Biotechnol. 2020;8:290.
[34] Sui T, Salvati E, Zhang H, Dolbnya I, Korsunsky A. Multiscale synchrotron scattering studies of the temperature-dependent changes in the structure and deformation response of Mater Today Adva thermoplastic polyurethane elastomer. Mater Today Adv 2019;4:100024.
[35] Kaushiva BD, Wilkes GL. Influence of diethanolamine (DEOA) on structure–property behaviour of molded flexible polyurethane foams. J Appl Polym Sci 2000;77(1):202–16.
[36] Gildner CD, Lerner AL, Hocking DC. Fibronectin matrix polymerization increases tensile strength of model tissue. Am J Physiol Heart Circ Physiol 2004;287(1):H46–53.
[37] Chernonosova VS, Gostev AA, Gao Y, Chesalov YA, Shutov AV, Pokushalov EA, et al. Mechanical properties and biological behaviour of 3D matrices produced by electrospinning from protein-enriched polyurethane. BioMed Res Int 2018;2018.
[38] Jin L, Zeng Z, Kuddannaya S, Yue D, Bao J, Wang Z, et al. Synergistic effects of a novel free-standing reduced graphene oxide film and surface coating fibronectin on morphology, adhesion and proliferation of mesenchymal stem cells. J Mater Chem B 2015;3(21):4338–44.
[39] Hidalgo-Bastida L, Barry J, Everitt N, Rose F, Buttery L, Hall I, et al. Cell adhesion and mechanical properties of a flexible scaffold for cardiac tissue engineering. Acta Biomater 2007;3(4):457–62.
[40] Rnjak-Kovacina J, Wise SG, Li Z, Maitz PK, Young CJ, Wang Y, et al. Tailoring the porosity and pore size of electrospun synthetic human elastin scaffolds for dermal tissue engineering. Biomaterials 2011;32(28):6729–36.
[41] Verma RP, Hansch C. Matrix metalloproteinases (MMPs): chemical–biological functions and (Q) SARs. Bioorg Med Chem 2007;15(6):2223–68.
[42] Qiu Y, Lim JJ, Scott jr L, Adams RC, Bui HT, Temenoff JS. PEG-based hydrogels with tunable degradation characteristics to control delivery of marrow stromal cells for tendon overuse injuries. Acta Biomater 2011;7(3):959–66.
[43] Kloxin AM, Kasko AM, Salinas CN, Anseth KS. Photodegradable hydrogels for dynamic tuning of physical and chemical properties. Science 2009;324(5923):59–63.